AD-A037 761 CALIFORNIA UNIV LOS ANGELES DEPT OF ELECTRICAL SCIEN--ETC F/G 20/9
EXPERIMENTAL SIMULATION OF PARAMETRIC INSTABILITIES IN LASER-PL--ETC(U)
NOV 76 N C LUHMANN F49620-76-C-0012

UNCLASSIFIED AFOSR-TR-77-0157 NL

| OF |
AD
A037761

END

DATE
FILMED
4-77

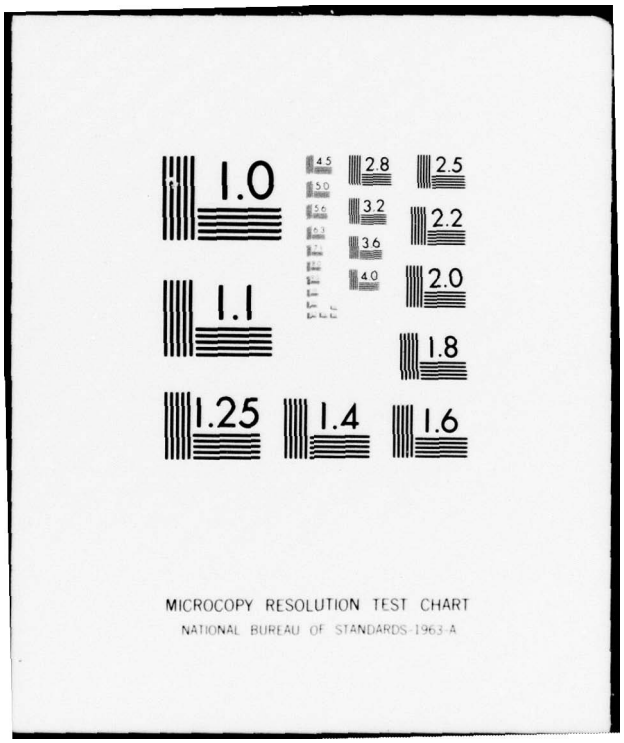
1.0
1.1
1.25
1.4
1.6
1.8
2.0
2.2
2.5
2.8
3.2
3.6
4.0
4.5
5.0
5.6
6.3
MICROCOPY RESOLUTION TEST CHART
NATIONAL BUREAU OF STANDARDS-1963-A

Work supported in part by the
U.S. Air Force Office of Scientific Research,
Contract F49620-76-C-0012
U.S. Energy Research and Development Administration
Contract E(04-3)-34, P.A. 236 and the
National Science Foundation
Grant ENG 75-14452

UCLA-ENG-7701
NOVEMBER 1976

EXPERIMENTAL SIMULATION OF PARAMETRIC INSTABILITIES IN LASER-PLASMA INTERACTIONS

N.C. LUHMANN, JR.

UCLA • SCHOOL OF ENGINEERING AND APPLIED SCIENCE

AIR FORCE OFFICE OF SCIENTIFIC RESEARCH (AFSC)
NOTICE OF TRANSMITTAL TO DDC
This technical report has been reviewed and is
approved for public release IAW AFR 190-12 (7b).
Distribution is unlimited.
A. D. BLOSE
Technical Information Officer

EXPERIMENTAL SIMULATION OF PARAMETRIC INSTABILITIES IN LASER-PLASMA INTERACTIONS*

N. C. Luhmann, Jr.
Electrical Sciences and Engineering Department
University of California
Los Angeles, California 90024

Paper presented at the U.S. - Japan Seminar on Laser Interactions with Matter, Rochester, New York, November 2-5, 1976

*Work supported in part by the U.S. Air Force Office of Scientific Research, Contract F49620-76-C-0012 the U.S. Energy Research and Development Administration, Contract E(04-3)-34, P.A. 236 and the National Science Foundation, Grant ENG 75-14452.

I. INTRODUCTION

There is currently a great interest in the mechanisms by which intense electromagnetic radiation interacts with plasmas. A major impetus for this interest has been the laser-pellet fusion program. The process whereby the incident electromagnetic wave gives up energy to the plasma can be much more complex than simple binary collisional damping by electron-ion collisions.

Even for relatively weak electromagnetic fields, the electrons acquire a quiver velocity which can be a few percent of their thermal velocity. The resulting charge separation can supply an energy source for instability. The long wavelength driving electric field can provide, for example, a coupling between electron plasma oscillations and ion acoustic waves of the same wavenumber, and they may grow together with the energy supplied by the external field. These waves, in general, have much larger wavenumbers (slower phase velocities) and are subject to much larger Landau damping than the pump wave, leading to so-called anomalous absorption. Therefore, the conversion of laser radiation energy to plasma heat occurs through classical inverse bremsstrahlung, augmented by resonant absorption and parametric decay processes at the critical layer ($\omega_o = \omega_p$) and the quarter-critical layer ($\omega_o = 2\omega_p$). Both computer simulations and microwave experiments have shown that these parametric processes can produce large tail heating of the electron distribution. These suprathermal electrons can penetrate the core of the cold DT pellet making compression of the pellet much more difficult (preheat). A related problem is that fast electrons do not efficiently couple their energy into the outer layers of the pellet, thereby reducing the compression (decoupling). Absorption at the resonance layer can also lead to caviton formation and profile modifications. Fast ions can also be generated during anomalous absorption

processes and have accounted for as much as 80% of the absorbed laser light in some experiments. The production of fast ions therefore constitutes a serious loss mechanism for irradiated pellets. In addition to the decay instabilities, the backscattering parametric instabilities--stimulated Brillouin scattering (SBS), stimulated Raman scattering (SRS), and stimulated Compton (SCS)--can occur in the underdense region outside the critical layers, preventing efficient absorption of laser light. The backscattered light in target experiments has ranged from 10% to 50% of the incident intensity.

Direct comparison between theoretical predictions and laser-pellet experiments is hindered by the small size and short time scale of these experiments. Therefore, we have chosen to perform experimental simulations in larger, less dense plasmas in order to elucidate those processes of importance to laser-fusion. We will discuss two examples of such experimental simulations which were performed in our laboratory. In the first experiment, the proposed control of parametric instability produced suprathermal electrons has been investigated using high power microwaves in a large, tenuous plasma. The second experiment to be discussed involves the study of the reflective instability using an underdense plasma irradiated by a CO_2 laser.

A third experiment, recently underway, is the study of self-focussing instabilities in plasmas using both far-infrared lasers and pulsed microwave sources.

II. Parametric Instability Control Using Finite-Bandwidth Pumps

As mentioned earlier, the absorptive instabilities[1] (parametric decay and oscillating two-stream) can produce nonthermal, hot electrons which can prevent the successful realization of laser-pellet fusion. The hot electrons

can penetrate the core and impede the compression of the pellet (preheat)[2]. There has therefore been considerable interest in means to increase the instability thresholds and decrease the growth rates.

A proposed method to control parametric instabilities is to properly shape the bandwidth characteristics of the incident electromagnetic radiation. Theoretical investigations[3-8] and computer simulation[9] have indicated that a finite bandwidth pump can significantly increase the threshold power and reduce the growth rates for parametric instabilities. The physical mechanism responsible for this control is illustrated in Fig. 1. Figure 1(a) depicts the threshold power for parametric instability as a function of the frequency of a narrowband pump. The instability resonance width is characterized by the quantity γ. The lower graph typifies the Fourier power spectrum of a finite bandwidth pump. If the bandwidth $\Delta\omega$ is much larger than the instability resonance width γ, the effective power available to excite the instability is related to the incident power P_o by $P_{eff} = \gamma/\Delta\omega$. The effective power is illustrated in Fig. 1(b) by the cross-hatching. More rigorous theoretical treatments[3,9] have tended to support this simple intuitive model. However, the majority of this work has been concerned with the effects of finite pump bandwidth on only a few coupled modes. More recently, a weak turbulence treatment of the problem has been published[10]. Space and time limitations preclude a detailed discussion of the various theoretical approaches. However, we note that there appears to be some disagreement about whether the actual mechanism responsible for the finite bandwidth is important. Tamor[8], for example, has noted that there should be a difference between coherent and incoherent bandwidth mechanisms on the excitation of the parametric decay instability. Other authors find that in the limit of large bandwidth, the particular mechanism is unimportant[3]. We also note that a complete theoretical

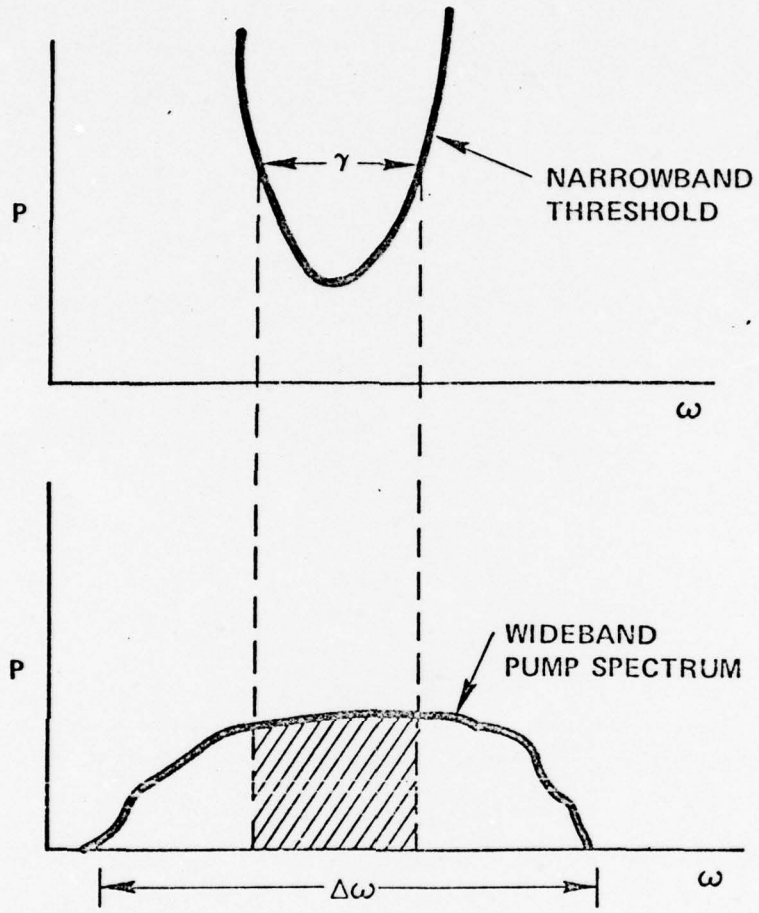

Fig. 1 Illustration of finite bandwidth pump control of parametric instabilities. (a) The narrowband threshold curve is indicated as a function of pump center frequency. (b) The power spectrum of a broadband pump is shown with the "effective" power indicated by the cross-hatched region.

treatment of the actual conditions with pump depletion, mode coupling, plasma inhomogenities, finite interaction length, etc. is quite difficult. We have therefore chosen to investigate the problem experimentally in the microwave region.

An additional motivation for undertaking a microwave experimental simulation of the effects of finite bandwidth was the results of the experiment by Yamanaka et al[11]. In this work, the plasma heating due to both a broad-band laser (Nd-glass oscillator) and a narrowband laser (YAG oscillator) was studied. In consrast to theory[3-9] it was found that the broadband laser was more effective in heating the plasma. This result was attributed to the double pump resonance effect discussed by Arnush et al[12]. They find that two pumps can, under certain conditions, reduce the threshold for both the parametric decay and the oscillating two-stream instabilities.

In order to resolve such questions, as discussed above, we designed two microwave experiments. In the first experiment, the instability was excited electrostatically be means of an rf excited gridded capacitor plate structure immersed in a low density plasma ($n_e \simeq 10^{10}$ cm^{-3}). In this relatively low power experiment ($P \lesssim P_{th}$), we examined the effects of finite bandwidth on the threshold and growth rate of the instability produced Langmuir and ion acoustic waves. In the second experiment, the parametric instability was excited by freely propagating microwave radiation launched by means of a gridded waveguide horn into a near critical density plasma. For these latter studies, sufficient power levels were employed to observe instability produced fast electrons.

IIA. Instability Excitation by an Electrostatic Pump

Figure 2 depicts schematically the experimental apparatus used in this investigation. An unmagnetized, electrostatically confined[13,14] plasma of 100 cm length and 35 cm diameter is produced by a filament discharge with argon fill pressures of 0.4 mTorr. Typical plasma parameters are electron temperature $KT_e \simeq 2\text{-}3$ eV, temperature ratio $T_e/T_i \simeq 8\text{-}10$, plasma density $n_e = (2\text{-}18) \times 10^9$ cm^{-3} and total background fluctuation level $\Delta n/n < 0.1\%$. The rf pump is introduced by means of a gridded parallel-plate capacitor system (5 cm diameter, 3 cm spacing, mesh constant $\simeq 5\lambda_{De}$) similar to that of Stenzel and Wong[15]. The grids produce a slight local density depression with a density gradient of $\simeq 2\%$/cm. over several centimeters from the grids. Shielded double and single Langmuir probes are employed to monitor plasma parameters and to detect instability produced plasma waves.

Upon application of narrowband rf power to the grids, a well-defined ion disturbance ($\Omega_i/2\pi \simeq 400$ kHz) appears when the power exceeds a distinct threshold value and the frequency is near the electron plasma frequency ($\omega_o > \omega_{pe}$). Figure 3 shows a spectrum analyzer presentation of the low frequency spectrum together with the corresponding high frequency decay spectrum for a power level considerably above threshold. As the power is increased, the spectrum becomes broad and turbulent as indicated in Figure 4. The observed value of the threshold power together with frequency matching ($\omega_o = \omega_e + \Omega_i$) and propagation velocity measurements indicate that the parametric decay instability is excited by the pump. It should be noted that the observed most unstable ion wave yields a value for $k\lambda_{De} \simeq 0.1$ which is smaller than that predicted by the homogeneous theory ($k\lambda_{De} \simeq 0.18$). This is probably due to convective losses which would favor the excitation of decay waves with lower group velocity (smaller $k\lambda_{De}$). The growth of the ion acoustic wave is shown

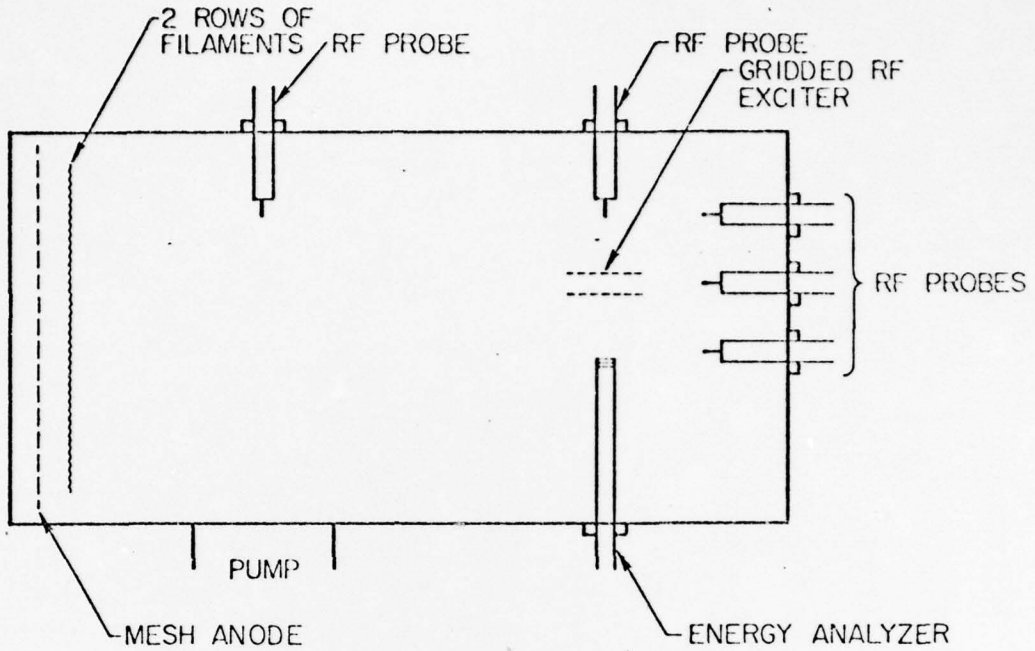

Fig. 2 Schematic of experimental apparatus used to investigate the effects of a finite bandwidth pump on the parametric instability produced decay waves.

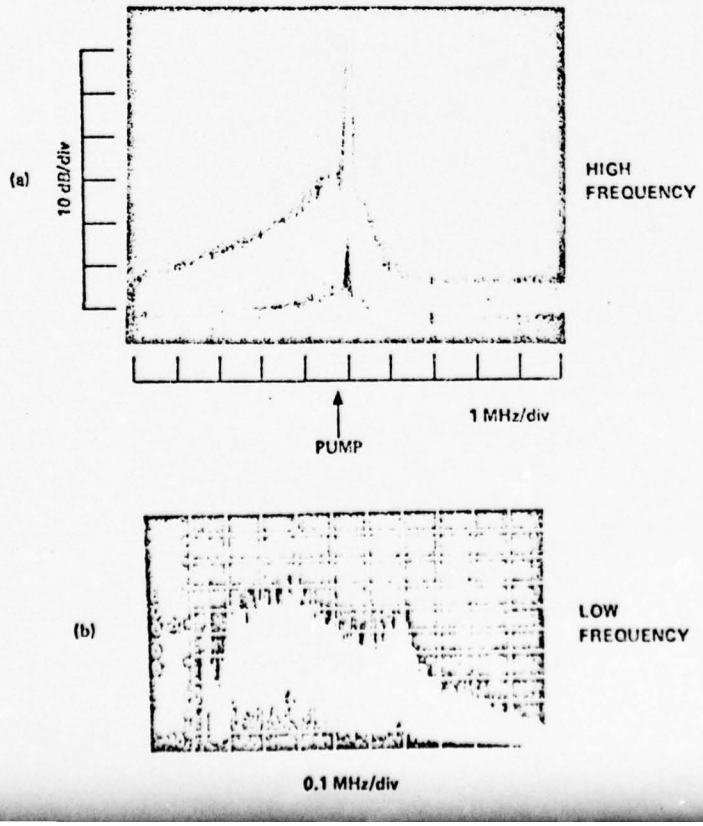

Fig. 3 Spectrum analyzer traces of the Langmuir (a) and ion decay waves (b) produced by a narrow-band pump.

in Fig. 5 when the rf source is pulsed. The finite propagation time to the probe and the persistance of the oscillation after cessation of rf excitation agree with the ion acoustic velocity for our plasma ($C_s \simeq 2.3 \times 10^5$ cm/sec).

The resonance width of the instability, as determined by a narrow-band pump, is typically 3% of the pump center frequency. Here the resonance width is defined as the full width of the threshold power curve at the twice-power points where threshold fluctuation levels are defined as $\frac{\Delta n}{n} > 0.05\%$. The resonance width calculated from uniform plasma theory is $\sim 4\%$.

Several different finite-bandwidth pumps were employed in this experiment. By operating in the microwave region, we were able to precisely control the pump characteristics and make detailed comparisons with theory. In one scheme, finite bandwidth was produced by random amplitude modulation of the pump using Gaussian white noise. In a different approach, a pump was produced whose bandwidth is due primarily to phase modulation. The rf field of this source is given by $E(t) = E_o \cos(\omega_o t + \alpha(t)$ where $\alpha(t)$ is the particular phase modulation function. The attendant amplitude modulation was held to less than 20% for the random phase modulated pumps.

Figure 6 displays the observed ion acoustic fluctuation level for both a narrowband and a noise amplitude modulated ($\frac{\Delta\omega}{\omega} \simeq 4\%$) pump. In each case the pump center frequency was adjusted to coincide with the value for minimum threshold. Here A is the mean density fluctuation level in the frequency range of the instability produced ion waves [$\sim 0.1 - 1$ MHz]. A definite reduction in the saturated ion fluctuation level is observed to occur for the wideband pump.

The effect (on the power required to obtain various density fluctuation levels) of varying the noise pump bandwidth is presented in Fig. 7 where the bandwidth $\frac{\Delta\omega}{\omega}$ ranges from essentially zero to $\sim 4\%$. The lowest amplitude,

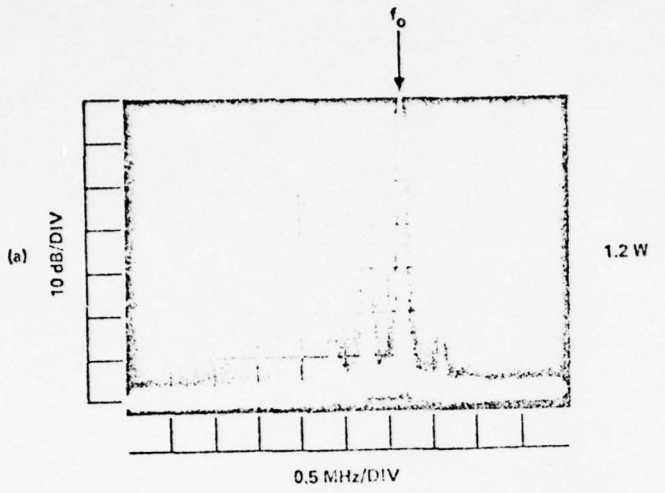

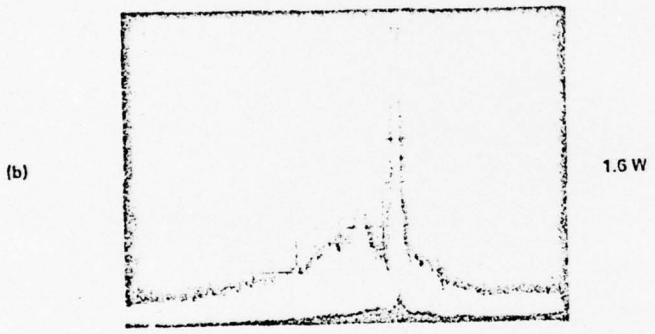

Fig. 4 Spectrum analyzer traces of the high frequency decay waves produced by a narrowband pump at two power levels.

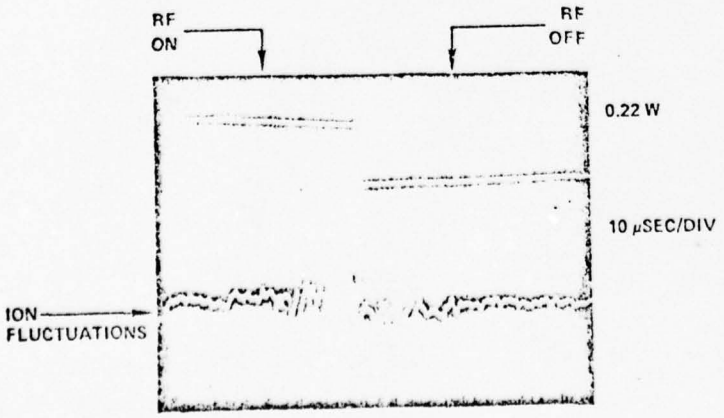

Fig. 5 Time evolution of instability produced ion waves detected by a double probe.

$A = 0.1\%$, corresponds to the threshold level where the instability first appears distinctively above the background fluctuations. In the limit $\Delta\omega >> \gamma$, theory[3-9] predicts that the threshold power and pump bandwidth $\Delta\omega$ are linearly related. Over the range of power levels and bandwidths investigated, this relation was found to be approximately satisfied not only for the instability threshold power, but also for the power necessary to achieve a given level of saturated density fluctuations. The straight line fit to the data presented in Fig. 7 is evidence of the validity of the theory. The nonzero intercept of the lines for $\Delta\omega = 0$ is indicative of the limitations of the theory which does not take account of the precise interaction of the pump at frequencies outside the resonance region. An estimate of the instability resonance width at each fluctuation level may be obtained from the slope of the lines in Fig. 7. Alternatively, the resonance width may be obtained directly by varying the frequency of the narrow-band pump and observing the width of the instability curve at the twice-power points for a given fluctuation level. The results obtained from both techniques are compared in Table I and are found to be in reasonable agreement.

TABLE I. Instability resonance width $\Delta\omega/2\pi$

Fluctuation level (%)	Resonance width[a] (MHz)	Resonance width[b] (MHz)
0.1	25	16
0.2	14	8
0.3	8	6

[a]Resonance width determined using narrow-band pump.

[b]Resonance width obtained from slopes in Fig. 7.

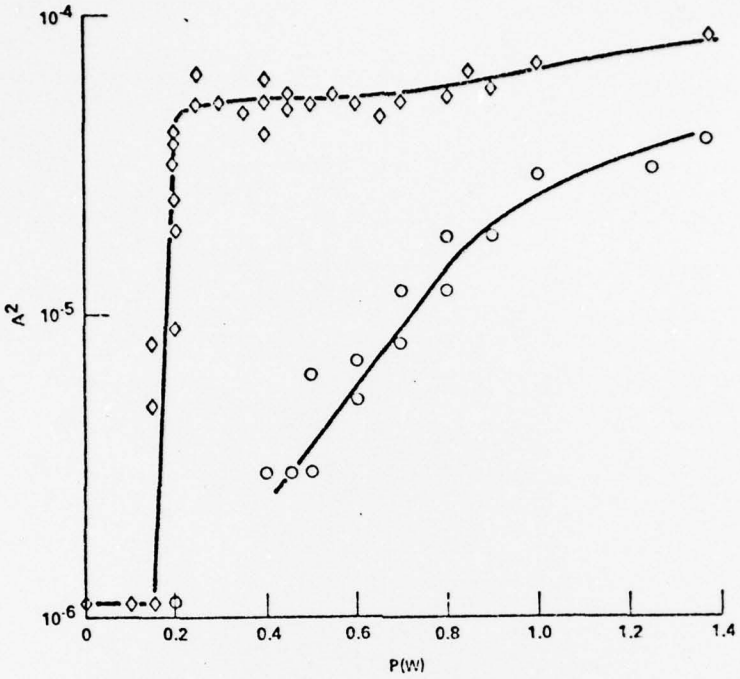

Fig. 6 Saturated ion acoustic fluctuation level for a narrowband pump (◇) and a noise amplitude modulated pump (○) with bandwidth $\Delta\omega/\omega_o \simeq 4\%$.

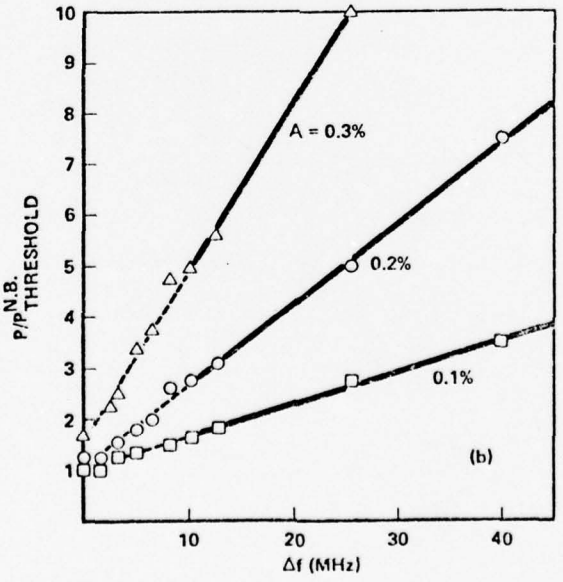

Fig. 7 Pump power (normalized to the narrowband threshold) required to produce a given density fluctuation level A as a function of the width of the noise amplitude modulated pump.

We have also examined the effects of finite bandwidth on the saturated level of the instability as a function of pump power and center frequency. Figure 8 shows the average ion density fluctuation level A for several noise pumps whose bandwidth is due to noise phase modulation. The width $\Delta\omega/\omega_o$ of the noise phase-modulated pump is varied from ~ 0% to 1.2% in Fig. 8, while the pump power is increased from 0.5 to 2 W in 0.5 W increments. Increased thresholds and decreased saturated levels are evident as the bandwidth is increased beyond the instability resonance width. Note that in this case, the bandwidth is due to a distinctively different mechanism from the previous results, where the pump was amplitude modulated. The similarity of the results for random amplitude and phase modulated pumps in the large bandwidth limit ($\Delta\omega > \gamma$) is in agreement with theory.

We have also employed another broadband pump where the bandwidth mechanism is coherent, and the spectral power distribution is discrete rather than continuous. For the case of sinusoidal phase modulation, the rf electric field is given by $E(t) = E_o\cos(\omega_o t + X\sin\omega_m t)$ where ω_m is the modulation frequency and X is the modulation index. The Fourier amplitude spectrum of this pump may be expanded in terms of Bessel functions. Its spectrum consists of the fundamental with amplitude proportional to $J_o(X)$ and modulation sidebands of amplitude $J_n(X)$ and frequency $\omega = \omega_o \pm n\omega_m$, where n is an integer. This is shown in Fig. 9 where we illustrate the possible effects of using such a pump with $\omega_m > \gamma$ to control parametric instabilities. An improper choice of center frequency could in some cases increase the instability level.

In Fig. 10 we present the experimental results where the sinusoidally phase modulated pump is tuned to resonance center and $\omega_m >> \gamma$. Here we plot

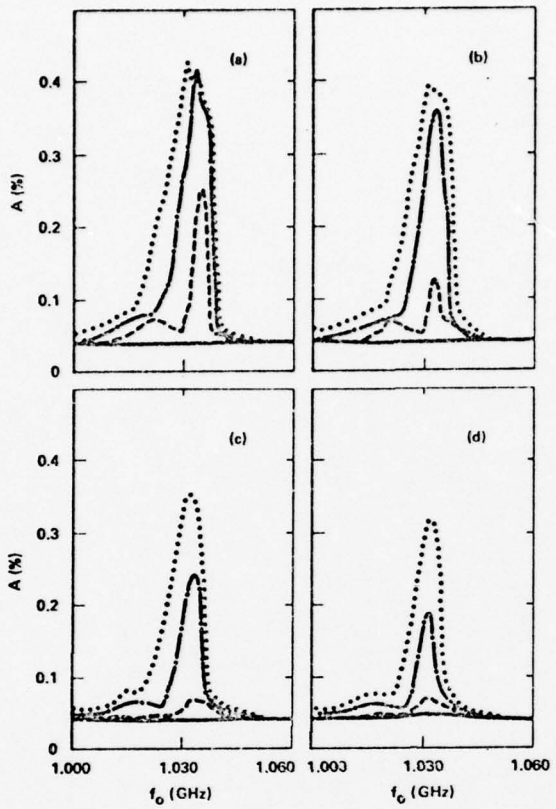

Fig. 8 Saturated density fluctuation level A as a function of pump power and center frequency for the noise phase-modulated pump. The noise bandwidth $\Delta\omega/2\pi$ is < 10 kHz for (a), 3 MHz for (b), 6 MHz for (c), and 12 MHz for (d). Pump power is varied from 0.5 to 2.0 W: ——, 0.5 W; ---, 1.0W; -·-, 1.5 W; and ···, 2.0 W.

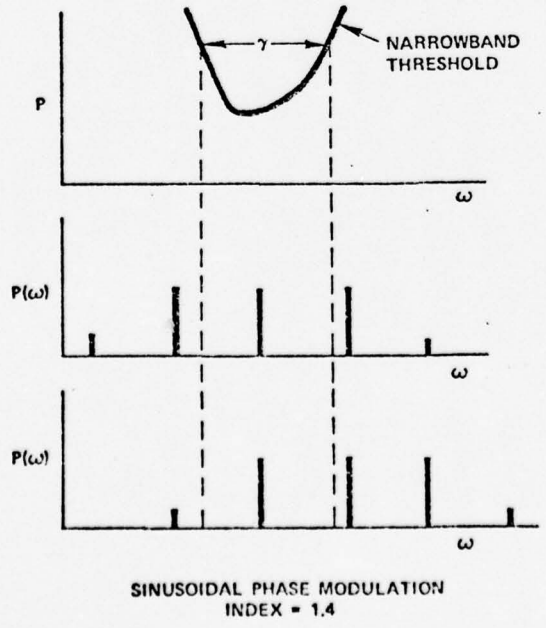

Fig. 9 Illustration of the effects of a sinusoidally phase modulated pump on the parametric instability. (a) Narrowband threshold power as a function of pump frequency. (b) Fourier spectrum of sinusoidally phase modulated pump with center frequency coincident with threshold minimum. (c) Modulation sideband coincident with threshold minimum.

the normalized threshold power as a function of the modulation index x. The power contained within the fundamental center lobe is proportional to $J_o^2(x)$. Therefore, simple theory predicts that the threshold power is proportional to $1/J_o^2(x)$:

$$P_{thres}(x) = J_o^{-2}(x) P_{thres}(o)$$

The solid line in Fig. 10 is the theoretical result (i.e., simply a plot of $J_o^{-2}(x)$ while the points are our experimental results. There are no "fitted" points. This result was obtained theoretically by Thomson and Karush[5].

We have also examined the results of sweeping the center frequency of a sine modulated pump through the instability resonance. In Fig. 11, we display the saturated amplitude of the ion fluctuations as a function of pump center frequency for several power levels. Here the modulation frequency ω_m is comparable to the instability resonance width γ. The modulation index is zero for Fig. 11(a), i.e., the narrow-band case, and increases in Figs. 11(b-d). In Figs. 11(c) and 11(d) where the modulation index is large, we see an apparent offset of the resonant frequency as the pump sidebands pass through the instability resonance.

We also investigated the effects of finite bandwidth on the growth of the instability. For the case $\gamma >> \Delta\omega > \gamma_o$, where γ_o is the instability exponentiation rate, we observed no change in growth rate when using either coherently or incoherently modulated pumps. Figure 12 shows the growth of the ion decay waves for both a narrow-band pump and a coherently modulated sine pump ($\omega_m \simeq \gamma$). At the lower power (Fig. 12(a)) finite bandwidth completely eliminates the instability, while at higher powers (Fig. 12(b)) it slows the growth rate.

We also examined the effects of finite bandwidth on the instability spectra. In Fig. 13, the spectral power distribution in the ion fluctuations

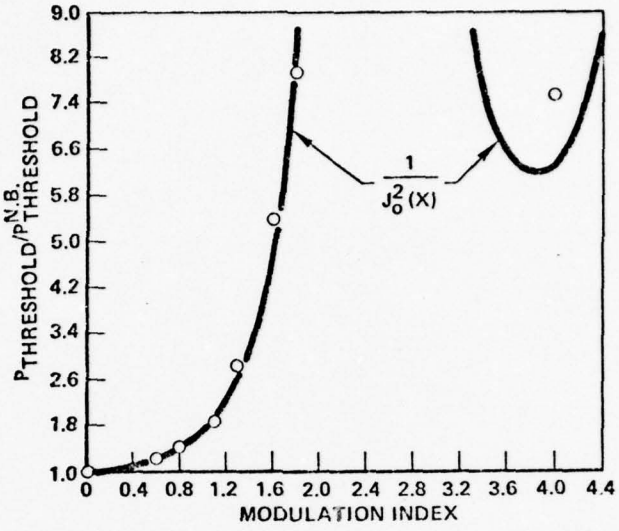

Fig. 10 Threshold power normalized to the narrowband threshold as a function of modulation index for a sinusoidally phase modulated pump ($\omega_m > \gamma$). Solid curve is $J_o^{-2}(x)$.

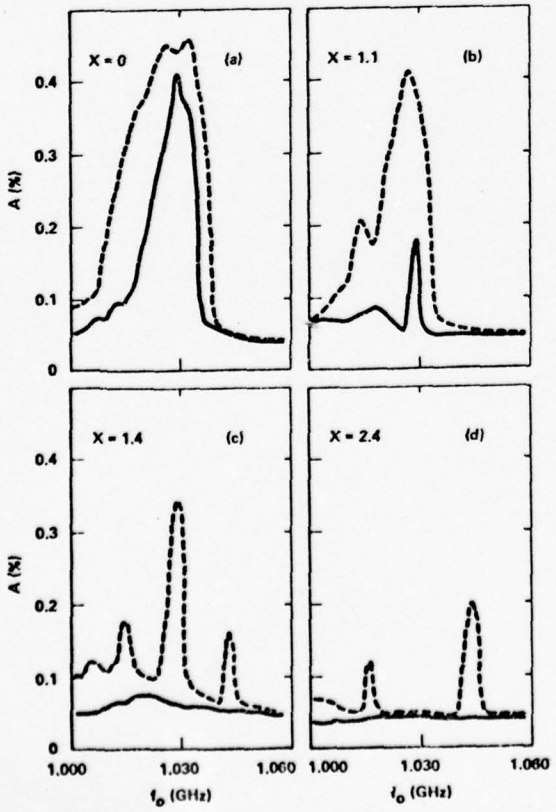

Fig. 11 Saturated density-fluctuations level A as a function of pump power and center frequency for the sinusoidally phase-modulated pump ($\omega_m/2\pi$ = 14 MHz > $\gamma/2\pi$). The modulation index is x = 0 for (a), x = 1.1 for (b), x = 1.4 for (c), and x = 2.4 for (d). For x = 1.4 the pump power is distributed approximately equally between the center frequency and the first upper and lower modulation sidebands, while for x = 2.4 the power at the center frequency is approximately zero. Two values of pump power are shown: ——, 2.0 W, and ---, 4.0 W.

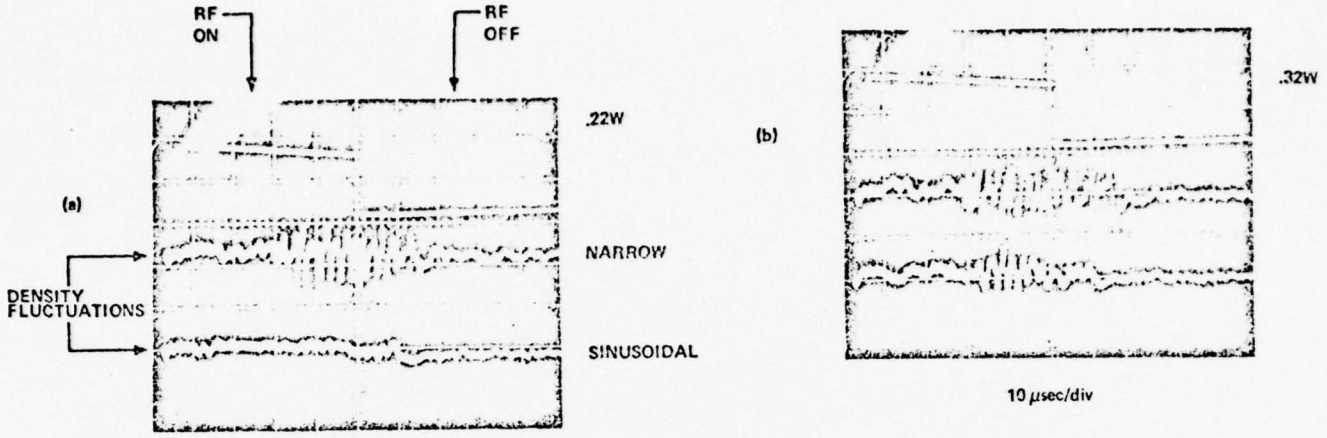

Fig. 12 Parametric instability produced density fluctuations for a narrowband pump and a coherently modulated sine pump ($\omega_m \simeq \gamma$).

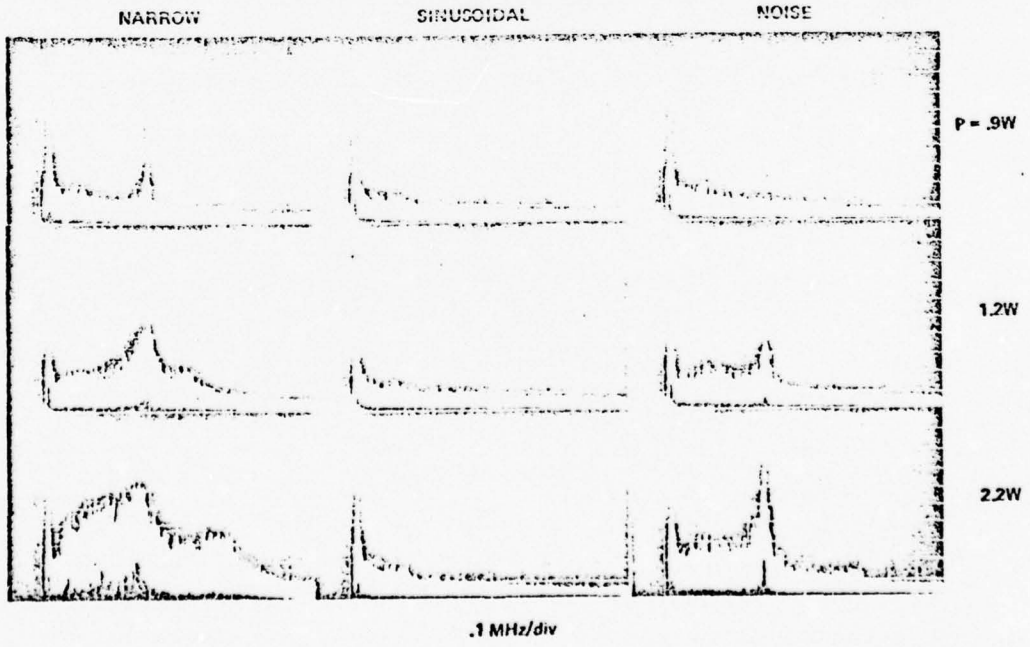

Fig. 13 Low frequency decay spectrum for a narrowband pump, a sinusoidally phase modulated ($\frac{\omega_m}{2\pi} \simeq \gamma$, x = 1.4) pump, and a noise phase modulated pump ($\Delta\omega \simeq \gamma$).

is shown for a narrowband pump, a sinusoidally phase modulated ($\frac{\omega_m}{2\pi} \simeq \gamma$, X = 1.4) pump, and a noise phase modulated pump ($\Delta\omega \simeq \gamma$). At higher powers, the modulated pumps produce instabilities whose spectral structure is similar to that of the narrowband pump at lower power. Note in particular the sharp ion mode ($\frac{\Omega_i}{2\pi} \simeq 400$ kHz) for the wide pump despite the larger frequency spread in pump power ($\Delta\omega >> \Omega_i$). At smaller bandwidths ($\Delta\omega$, $\omega_m << \gamma$), the phase modulation produced no discernable effects on the ion wave spectra. Upon examination of the high frequency decay waves, we did find evidence that finite bandwidth does change the instability mechanism. For the case of sinusoidal phase modulation with $\omega_m < \gamma$, each of the main spectral components of the pump can have decay sidebands, indicating a higher order bootstrapping process as indicated in Fig. 14 for a pump power level near the threshold value. At higher power levels these multiple decay sidebands become broad and turbulent as shown in Fig. 15.

We can briefly summarize our results obtained with this lower power experiment. The ratio $\frac{\gamma}{\Delta\omega}$ is the determining factor for finite bandwidth control. There appears to be no difference between the coherent and incoherent pump results when $\Delta\omega >> \gamma$.

IIB. Parametric Instability with an Electromagnetic Pump

We wish now to discuss an investigation of the effects of finite pump bandwidth on parametric instability using a distinctively different experimental arrangement than that described in the previous section. The purpose of this additional experiment was two-fold. First, we wished to determine if the previously discussed finite bandwidth effects were strongly dependent upon the particular arrangement employed. Secondly, we wished to employ higher

pump power levels so that the effects of finite bandwidth on electron tail heating could be studied.

Figure 16 illustrates the apparatus employed for this experiment. The experiments were performed in an unmagnetized, electrostatically confined filament-discharge plasma[13,14] of 100 cm length and 35 cm diameter with argon fill pressures of 0.4 mTorr. The discharge anode was pulsed ($V_p \simeq 100$ V, $\tau_p \simeq 5$ msec) in order to obtain a plasma density (10^{11} cm^{-3}) corresponding to near critical density for the 2.5 - 3.5 GHz microwaves employed. The large electron-ion temperature ratio ($KT_e \simeq 2$ - 3eV, $T_e/T_i \simeq 8$ - 10) facilitated the excitation of the parametric decay instability. The electron distribution is bi-Maxwellian, with approximately 0.5% of the electrons contained in a high energy tail ($KT_e \simeq 20$eV) which arises from the primary electrons associated with the plasma production. The microwave power (risetime < 2 nsec, duration < 20 μsec, P < 1kW) was introduced perpendicular to the chamber axis by means of a gridded horn. The horn exit aperture is approximately one free space wavelength wide and extends 8 cm into the chamber. At the higher power level (≃ 1 kW), the vacuum electric field is ≃ 145 V/cm at the horn opening which corresponds to $\eta_o = E_o (4\pi n_o KT_{eo})^{-\frac{1}{2}} \simeq 0.2$. The plasma density as a function of the distance from the dielectric window located at the narrow (entrance) end of the microwave horn is displayed in Fig. 17. In addition to the radial density profile shown in Fig. 17, there is a density variation along the chamber axis resulting in a density gradient scale length of ≃ 30 cm at the position of the gridded horn. Unless otherwise stated, the results discussed herein are restricted to those in which the incident microwave electric field was aligned parallel to the chamber axis. The mean density of the pulsed plasma changes by less than 0.1% over the rf pulse duration. The corresponding change in plasma frequency is much less than the observed instability resonance width.

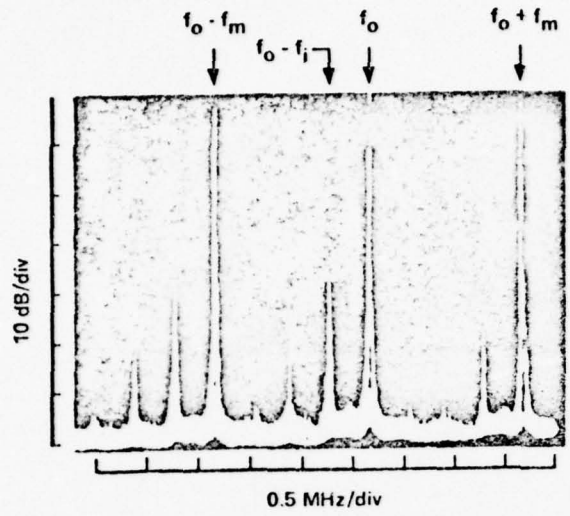

Fig. 14 High frequency decay spectrum near threshold for a sinusoidally phase modulated ($\omega_m < \gamma$) pump.

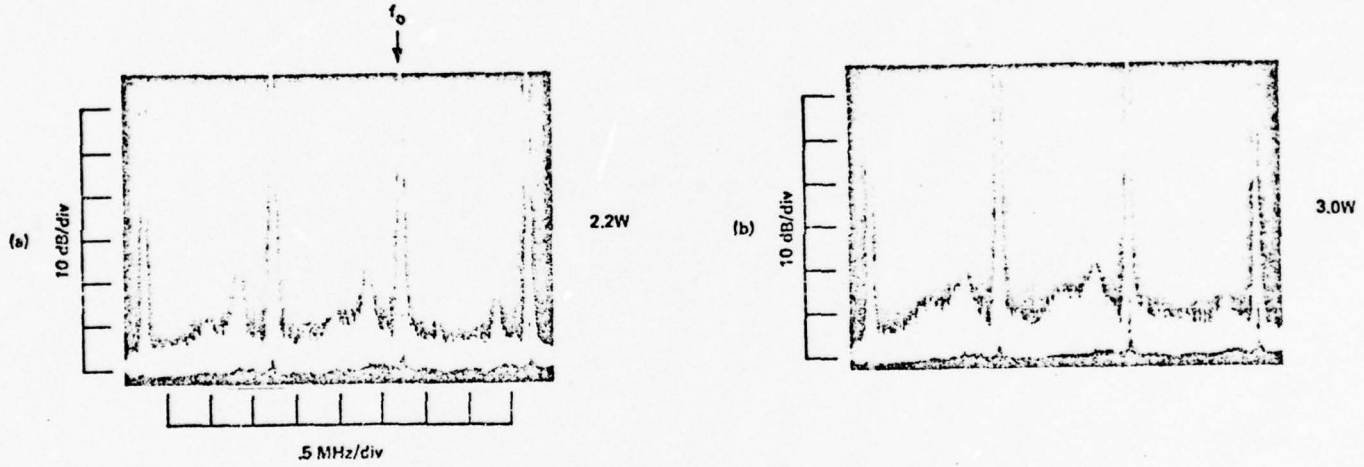

Fig. 15 Same conditions as in Fig. 14 but higher pump power.

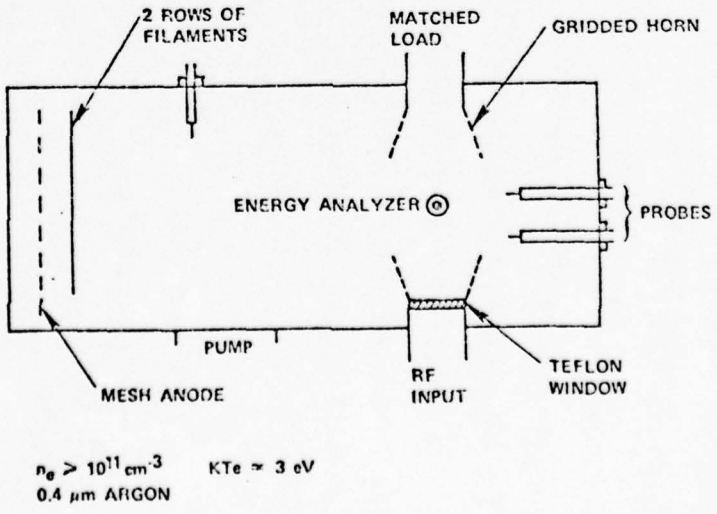

Fig. 16 Schematic of experimental apparatus employed to determine the effect of finite pump bandwidth on electron tail heating.

At moderate rf power levels ($P > 7W$ and $\omega_o \simeq \omega_p$) the low frequency density fluctuations and high frequency electric field fluctuations characteristic of the parametric decay instability are observed. The instability occurs within the uniform density region located 10 to 15 cm from the input window (see Fig. 17). The threshold power level of $\simeq 7W$ results in a vacuum electric field of $\simeq 12$ V/cm at the horn opening which corresponds to $\eta = E_o(4\pi n_o KT_e)^{-\frac{1}{2}} \simeq 0.02$ or $V_e/V_{th} \simeq 0.01$. Swelling of the pump can be neglected since the density gradient scale length is comparable to the vacuum wavelength of the pump. The growth of the instability produced density fluctuations is shown in Fig. 18 for a power level slightly above threshold. In Fig. 19, it is seen that finite bandwidth again reduces the amplitude and growth of the instability density fluctuations. The 10% bandwidth used in this result was obtained by random amplitude modulation.

To detect changes in the electron distribution function, movable multigrid electrostatic energy analyzers were employed. Upon instability onset, as detected by shielded Langmuir probes of both the double and single types, an increase in the hot electron current to the analyzers is observed. Using a rotatable analyzer, the energetic electrons are found to be preferentially directed along the electric field of the incident microwave radiation.

Upon varying the frequency of the narrowband pump and observing the instability produced hot electron flux ($|U_e| > 125$ eV) with the energy analyzers, we found that the resonance width γ for hot electron production increases from 2.4% of the pump frequency near threshold power to 5% at higher powers ($P \simeq 300W$). These results are presented in Fig. 20. Here we define γ as the frequency FWHM (at each power) of the saturated hot electron flux due to the instability. A simple extension of present theory[3-9] predicts that the pump bandwidth can have a significant effect on hot electron production

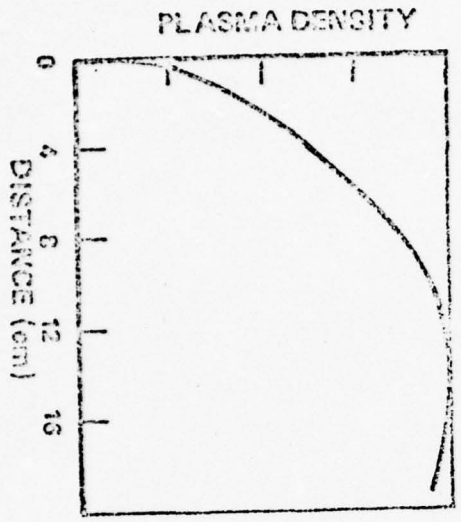

Fig. 17 Plasma density as a function of distance from the dielectric window located at the narrow (entrance) end of the microwave horn.

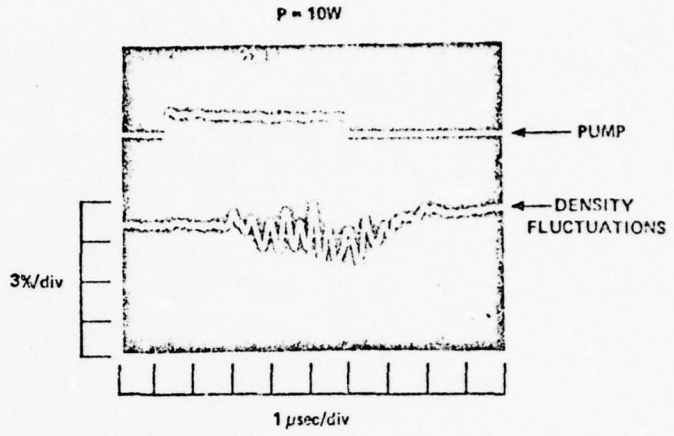

Fig. 18. Temporal evoluation of density fluctuations produced by a narrowband pump.

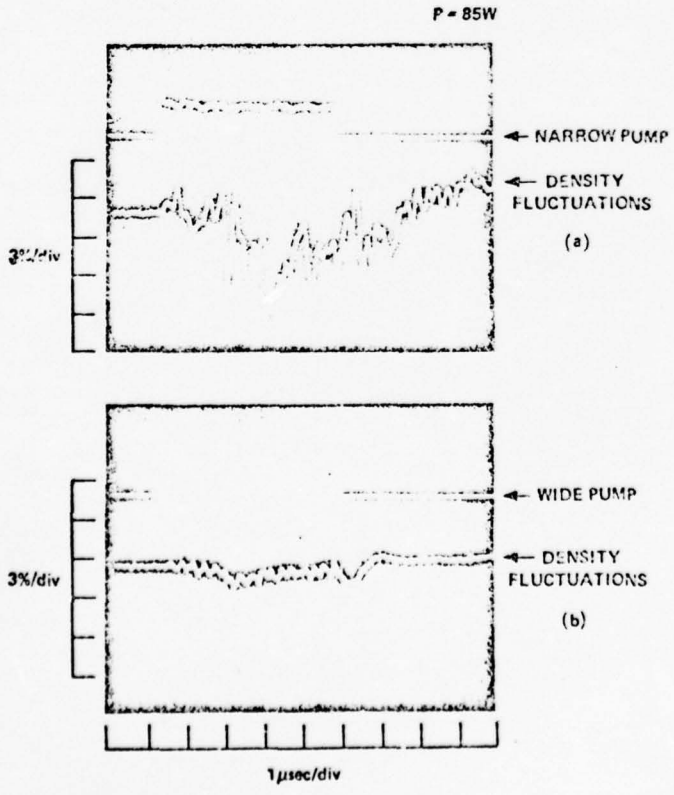

Fig. 19 Comparison of density fluctuations produced by a narrowband pump (a) and a noise amplitude modulated ($\frac{\Delta\omega}{\omega_o} \simeq 10\%$) pump (b).

when $\Delta\omega > \gamma$. This effect was investigated in the present experiment using both noise phase modulated pumps with bandwidths $\frac{\Delta\omega}{\omega_o}$ variable up to 1.2% and noise amplitude modulated pumps with bandwidths up to 23%. In both cases the noise employed is Gaussian white noise of adjustable amplitude and bandwidth. Figure 21 displays spectrum analyzer traces of noise amplitude modulated pumps of 40 MHz bandwidth ($\frac{\Delta\omega}{\omega_o} \simeq 1.3\%$) and 300 MHz bandwidth ($\frac{\Delta\omega}{\omega_o} \simeq 10\%$). Both pumps have a continuous spectral power distribution which is nearly constant (± 3dB) over the indicated bandwidth. The temporal evolution of the pulsed power of a narrowband pump, a noise phase modulated pump and a noise amplitude modulated pump are shown in Fig. 22.

Figure 23 shows the growth of the hot electron current to an energy analyzer for random amplitude modulated pumps with the same average power ($P \simeq 7\ P_{th}$), but with different bandwidths ($0 \leq \frac{\Delta\omega}{\omega_o} \leq 10\%$). In each case the pump center frequency was adjusted to coincide with minimum threshold for the narrowband pump. The reduction in hot electron production with increasing bandwidth are obvious.

In Fig. 24, the saturated level of parametric instability produced hot electron current is plotted as a function of pump bandwidth at several pump powers. The ambient current to the analyzer due to the aforementioned tail is not included here. In all cases, the pump center frequency was adjusted to coincide with that of minimum threshold for the narrowband pump. Note that at the lower power levels, where the instability resonance width γ is relatively narrow ($\frac{2\pi\gamma}{\omega_o} \simeq 2.4\%$), the wideband pumps effectively eliminate the hot electron current. At much higher power levels ($P >> P_{th}$), there is some reduction in hot electron current over the narrowband pump, but no elimination up to the maximum bandwidths employed ($\frac{\Delta\omega}{\omega_o} \simeq 23\%$). The slight increase in hot electron current shown in Fig. 24 for the higher powers and

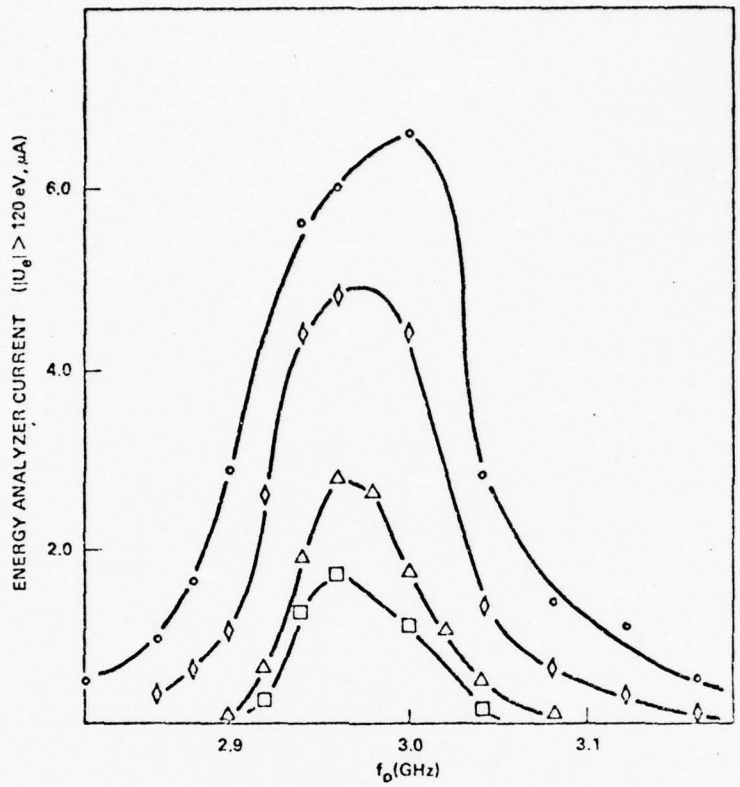

Fig. 20 Hot electron current ($|U_e| > 120$ eV) as a function of the narrowband pump center frequency: (□) 43W, (△) 85 W, (◊) 170 W and (○) 340 W.

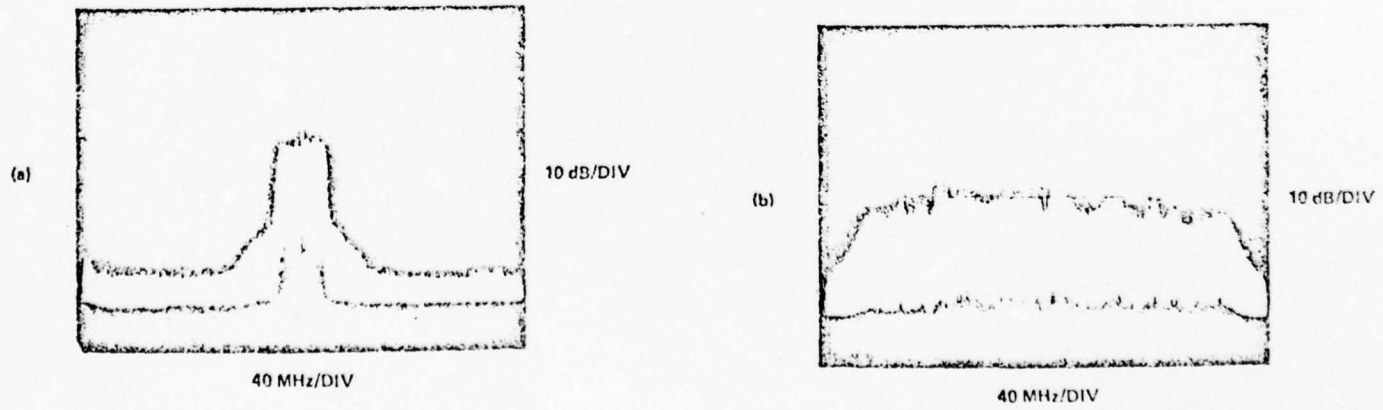

Fig. 21 Typical random amplitude modulated noise pumps. Pump center frequencies were ≈ 3GHz.

(a) (b) (c)

Fig. 22 Temporal evolution of the pulsed power of a narrowband pump (a), a noise phase modulated pump (b) and a noise amplitude modulated pump (c).

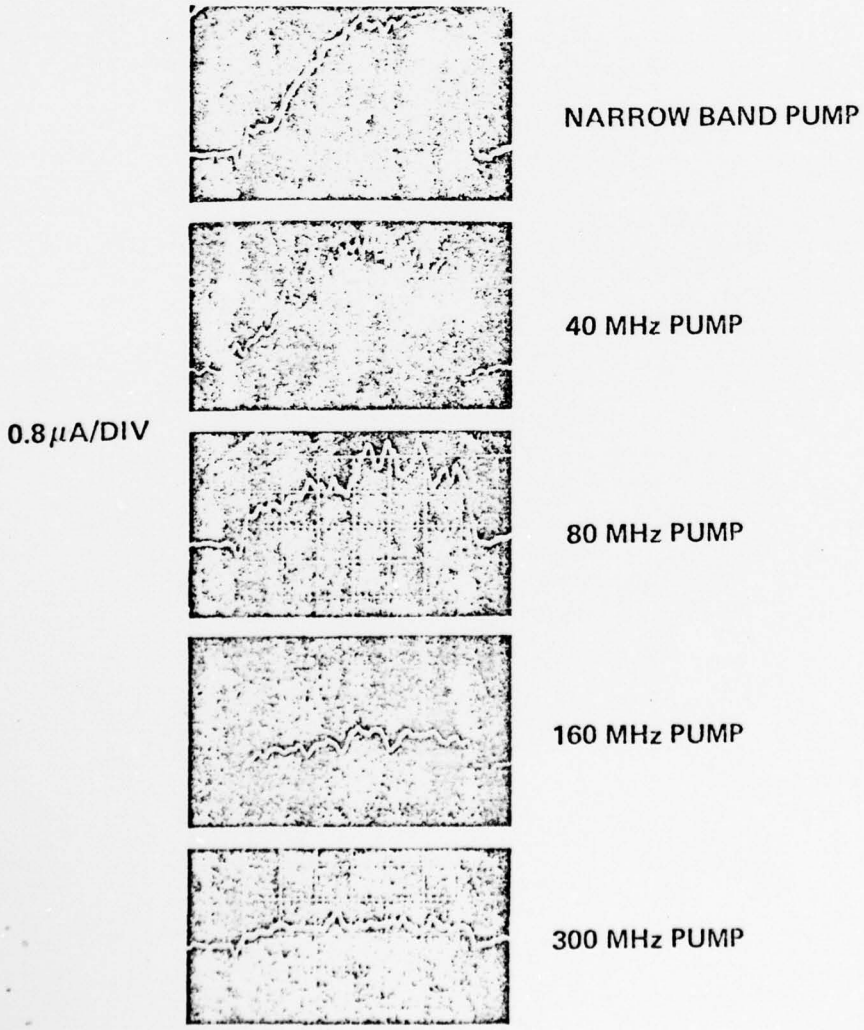

Fig. 23 Energy analyzer measurements (2μs/div) of the effects of finite pump bandwidth on the production of hot electrons.

moderate bandwidth pumps ($\frac{\Delta\omega}{\omega_o} \sim 1\%$) may be due to the slight shift in the instability resonance center which is observed to occur at high power (see Fig. 20). For the available bandwidths, little difference was observed in the saturated hot electron current due to either phase or amplitude modulated pumps of equal <u>average</u> power as long as $\Delta\omega >> \frac{2\pi}{\tau_g}$, where τ_g is the growth time for instability saturation. When the pump bandwidth is reduced ($\Delta\omega < \frac{2\pi}{\tau_g} < \gamma$), the phase modulated pumps yield hot electron currents indistinguishable from the narrow pump, while the amplitude modulated pumps produce an appropriately amplitude modulated hot electron current.

The saturated hot electron flux is shown in Fig. 25 for both the narrowband and 300 MHz ($\frac{\Delta\omega}{\omega_o} \simeq 10\%$) noise amplitude modulated pumps as a function of pump center frequency for several power levels. Near the instability resonance center frequency, the finite bandwidth pump is observed to reduce or even eliminate the analyzer hot electron current. However, at high power, the effective instability resonance width is seen to increase for the noise pump. In the case of the broadband pump, hot electrons are detected at pump center frequencies where none are observed with the narrow pump. This phenomenon may partially explain the increase in the instability amplitude observed by Yamanaka et al[11] in a finite bandwidth laser heating experiment.

The effect of finite bandwidth on the instability produced hot electron distribution function was investigated. For our plasma, the higher power narrowband pumps heat a fraction (< 10%) of the electrons in the 20eV tail of the initial electron distribution function to a higher temperature ($\sim$30eV) Maxwellian velocity distribution. Reductions in power mainly reduced the number of heated electrons, with only small changes in the final

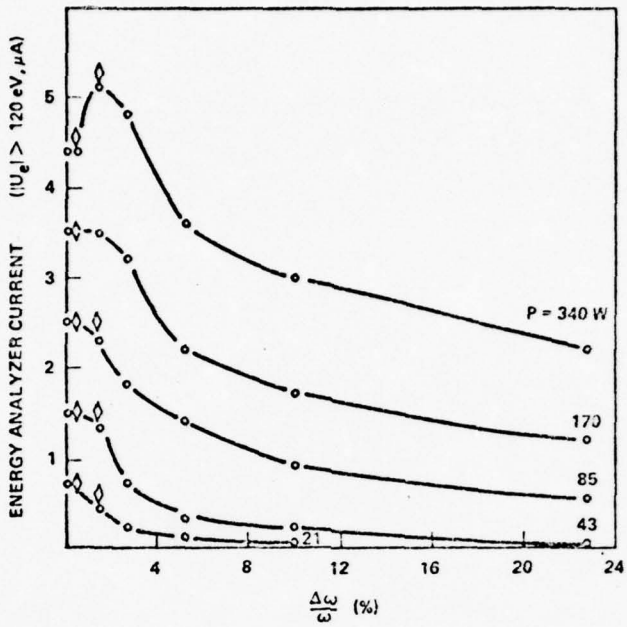

Fig. 24 Saturated level of hot electron current as a function of pump bandwidth: (◊) noise phase modulation, (○) noise amplitude modulation.

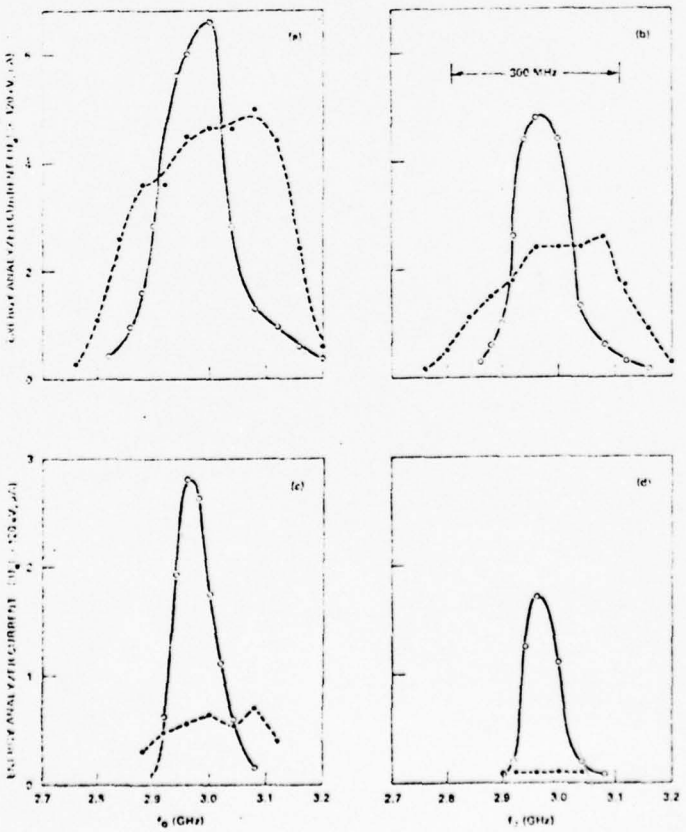

Fig. 25 Saturated level of hot electron current for a narrowband (○) pump and a 300 MHz ($\frac{\Delta\omega}{\omega_o} \simeq 10\%$) noise amplitude modulated pump (●) as a function of pump center frequenc : (a) 340 W, (b) 170 W, (c) 85 W, and (d) 43 W.

tail temperature. Similarly, we found that the finite bandwidth pumps simply decreased the maximum number of heated electrons, without changing the temperature of the heated electrons. The relatively small percentage of heated electrons, (< .1% of the total), may reflect the small size of the instability region in comparison to the hot electron mean free paths.

Figure 26 displays the time evolution of the hot electron current detected by an energy analyzer for both the narrow and noise modulated ($\frac{\Delta\omega}{\omega} \simeq 10\%$) pumps at several power levels. In each case, the pump center frequency coincided with that of minimum threshold for the narrowband pump. At low power levels ($P \lesssim 21W \simeq 3\ P_{th}$), there were no detectable hot electrons for the wideband pump, while electron tail heating was observed down to 7 W with the narrow pump. At higher powers, ($P \gtrsim 21W$) hot electrons are produced by both pumps and we can compare their respective rates for hot electron production. The initial fast growth in the hot electron current which saturates and begins to decay ~ 1 μsec after turn-on for the narrow pump (Fig. 26(a)) may be due to cavitation[16] or resonance absorption[17] arising from the plasma density gradient along the pump electric field. In the next paragraph, we breifly discuss the observed plasma density profile modifications which one would expect to occur with these instabilities. Finite pump bandwidth appears to drastically inhibit this early, quickly saturated hot electron production. Nevertheless, at the higher pump powers the average growth rate $\frac{dI_e^{hot}}{dt}$ for the hot electron flux produced by the wideband pump during the first few microseconds is comparable to or larger than that of the narrow pump. However, the hot electron flux consistently saturates at a lower level than for the narrow pump. When the pump center frequency is not adjusted to narrowband threshold minimum, the wideband pumps can have consistently faster growth rates for a given power than the narrowband pumps,

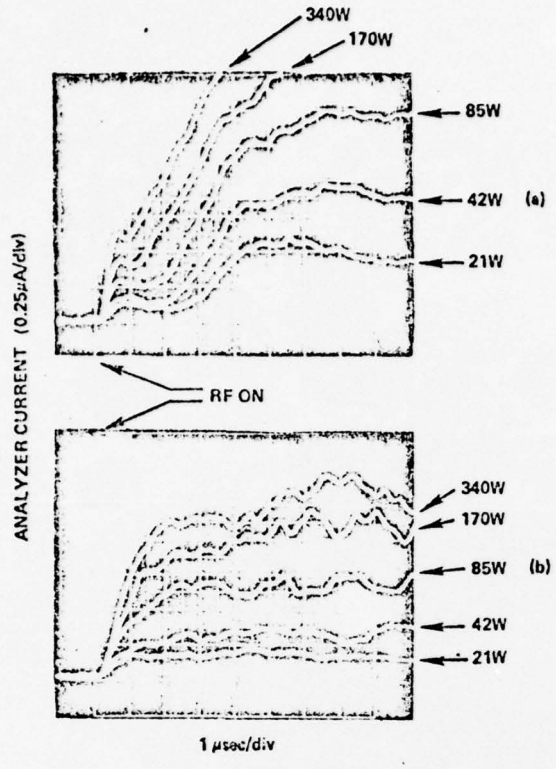

Fig. 26 Time evolution of the hot electron current ($|U_e| > 125$ eV) for the narrow pump (a) and the noise amplitude modulated ($\frac{\Delta\omega}{\omega_o} \simeq 10\%$) pump (b).

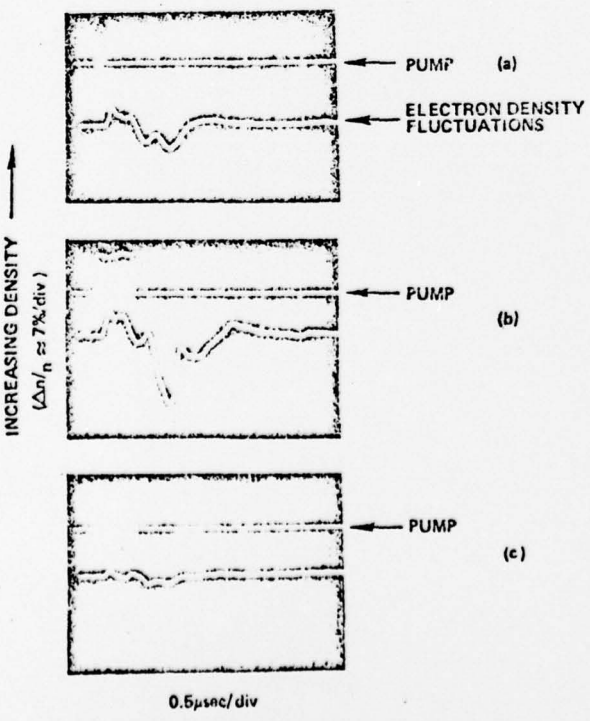

Fig. 27 Electron density fluctuations produced by short duration rf pulses: (a) and (b) narrowband pump, (c) noise amplitude modulated ($\frac{\Delta\omega}{\omega_o} \simeq 10\%$) pump.

similar to the saturation results of Fig. 25.

We have observed density cavities produced by short narrowband rf pulses, similar to those observed by Kim et al.[16] In Fig. 27(a), we show the electron density perturbation, as detected by a Langmuir probe biased to electron saturation, which occurred upon irradiating the plasma with a 150 nsec narrowband rf pulse at high power. Note that the density disturbance continues long after the rf pulse is turned off. Similar density perturbations, but with reduced amplitude, were observed for rf pulses as short as 40 nsec. Figure 27(b) shows the result of employing a longer narrowband pulse with the same power as in Fig. 27(a). Figure 27(c) shows the reduced density perturbation produced by the 300 MHz bandwidth noise pump with the same average power, pulse duration, and center frequency as the narrowband pump in Fig. 27(b). Coincident with the formation of these density cavities, bursts of hot electrons were observed to occur along the pump field. The hot electron flux produced by an 80 nsec duration narrowband rf pulse is shown in Fig. 28(a). The peak of the hot electron current, after accounting for instrumental delays, occurred 60 nsec after termination of the rf heating pulse. This period is long compared with the hot electron ($|U_e| > 120$eV) transit time to the analyzer ($\simeq$ 20 nsec). This delay is consistent with the occurrence of cavitation which leads to the persistence (trapping) of the rf fields. We have obtained similar results with pulse durations as short as 40 nsec; the peak electron current decreasing for pulses durations < 150 nsec. Figure 28(b) shows the results using a random amplitude modulated pump ($\frac{\Delta\omega}{\omega_o} \simeq 10\%$) with the same average power, pulse duration and center frequency as the narrowband pump used in Fig. 28(a). Both the bursts of hot electrons and the density cavities are found to be inhibited by finite pump bandwidth.

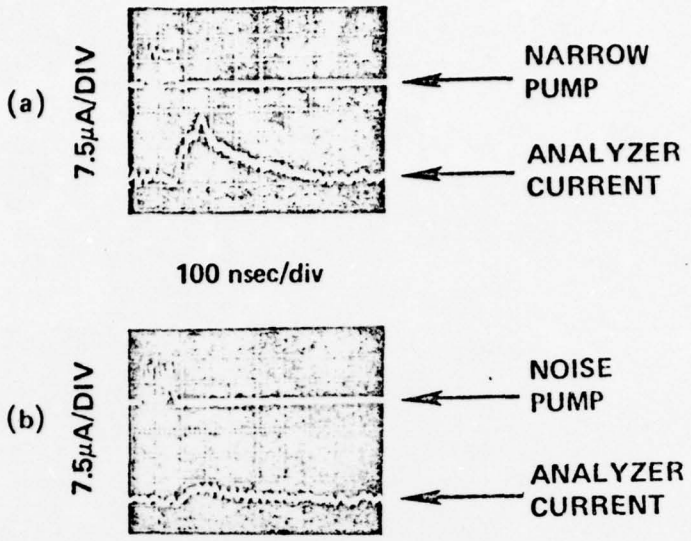

Fig. 28 Field aligned hot electron current ($|U_e|$ > 125 eV) associated with short duration rf pulses: (a) narrowband pump, (c) noise amplitude modulated ($\frac{\Delta\omega}{\omega_o} \simeq 10\%$) pump.

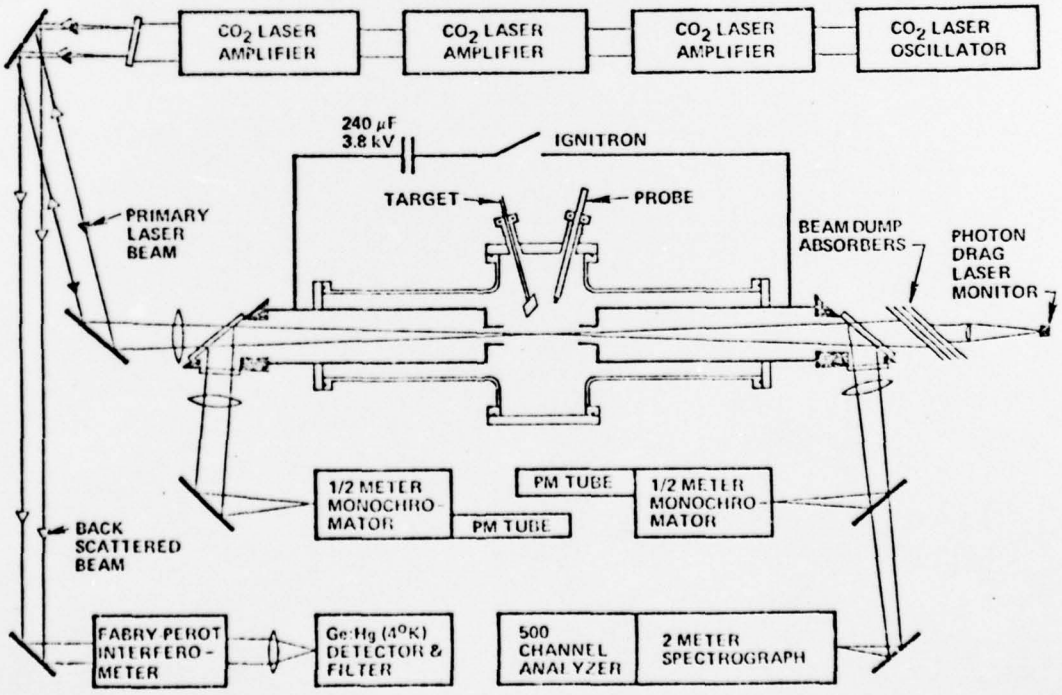

Fig. 29 Diagram of experiment to detect SBS in an underdense plasma.

In conclusion, we find that finite pump bandwidth can significantly increase the minimum threshold and reduce the saturation level of parametric instability decay waves and the associated suprathermal electrons. It also can apparently control the hot electron production due to cavitation. The fact that finite bandwidth did not produce a marked decrease in heating rates for nonthermal electrons on all timescales is somewhat surprising in view of present theory.

III. CO_2 Laser Experiments on Backscattering in Underdense Plasmas

Of great concern to proponents of laser-pellet fusion are instabilities which may occur in the outer underdense regions of the pellet causing reflection of incident laser energy. One such parametric instability is stimulated Brillouin scattering (SBS) in which the impinging electromagnetic wave drives an electrostatic ion wave unstable and Thomson scatters from it primarily in the backward direction. Extensive theoretical work in the literature gives the dependence of the threshold on plasma inhomogeneity length and finite interaction length[18,19,20,21]. Reflections observed from solid target experiments are not inconsistent with SBS, though a definite identification of the instability is complicated by plasma formation and expansion and by other reflective instabilities which occur at the quarter-critical and critical density surfaces.

At the UCLA Plasma Engineering Laboratory, an experiment was conducted to test the finite-length linear SBS theory in a plasma which was everywhere underdense. The experimental appartus is shown schematically in Fig. 29. The plasma was produced by a 30-kA discharge between hollow electrodes 1.9 cm i.d. and 10 cm apart with or without a 4 kG axial magnetic field. Typical

background plasmas of $n_e \approx 10^{16}$ cm^{-3} and $T_e \approx 4$ eV are created. A CO_2 laser chain consisting of a Lumonics 103 oscillator and three Dumanchin amplifiers produced a 45J, 50ns gain-switched pulse in a 3.2 cm diameter beam. When focused axially into the plasma by a 75 cm Ge lens, this beam produced an approximately uniform region of illumination 3 cm long and 0.1 cm in diameter with peak intensity 5×10^{10} W/cm^2. Backscattered light was collected by the same lens and routed by an NaCl beamsplitter to a Ge:Hg photoconductive detector through a Fabry-Perot interferometer. Two-channel on-axis spectroscopy allowed detailed investigation of plasma parameters before being irradiated by the laser and gave some indications of parameters during irradiation. In the latter case, a pit is burned in a lucite plate at the laser focus by a single attenuated oscillator pulse and illuminated by a CW He-Ne alignment laser to allow precise alignment of the spectroscopic channels to the CO_2 focal volume.

Stray light is 10^{-9} of incident power and sets the detection threshold. Typical time histories of stray and scattered light are shown in Fig. 30. Fig. 30(a) is a stray light signal from the photoconductor and Fig. 30(b) shows a spiky backscatter signal on the trailing edge. The delay between the laser peak and backscatter peak is attributed to the time history of plasma electron temperature due to laser heating. The peak electron-ion temperature ratio, corresponding to minimum SBS threshold, probably occurs some time after the peak laser intensity. In (c) may be seen some later backscatter followed by a smooth peak well out into the tail of the laser pulse. The cause of the later pulse has not yet been determined.

Before looking at Fabry-Perot scans of the backscattered spectrum, let us look at another check on the existence of the ion wave that would be characteristic of SBS. This is a direct means of observing the field at the

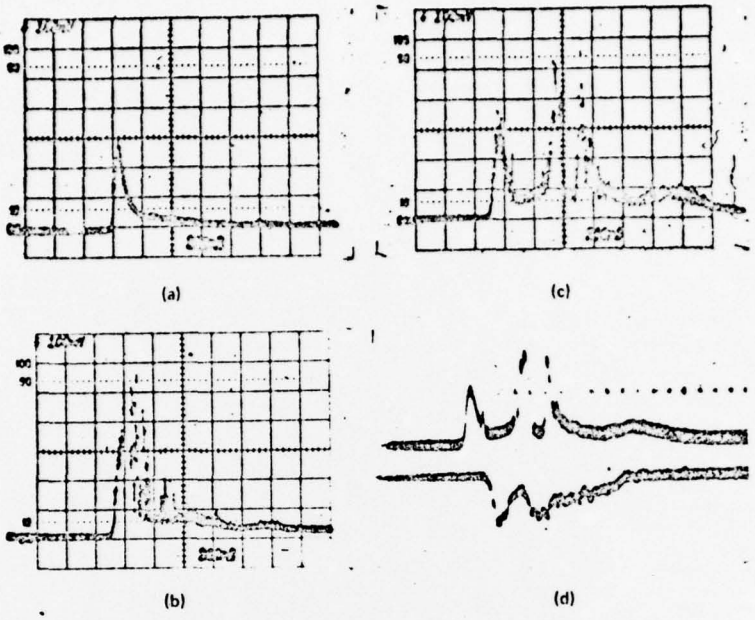

Fig. 30 Backscatter signals: (a) 10.6 μm stray light (plasma off); (b) typical backscatter plus stray light (plasma on); (c) same; (d) top trace: same pulse as (c) on 2-beam scope; bottom trace: 6632 A forbidden line signal (inverted). Sweep: 200 ns/div.

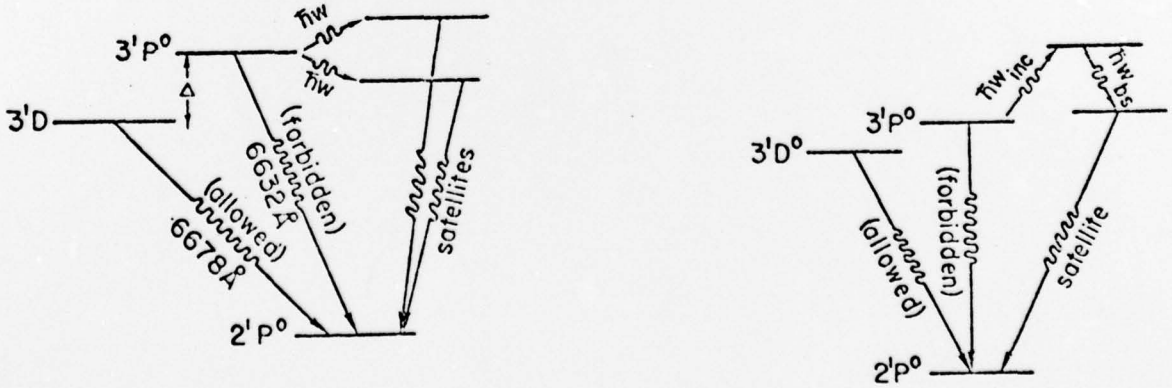

Fig. 31 Schematic of forbidden line diagnostic

low ion-wave frequency by the time-dependent Stark effect. A normally for-$3^1P - 2^1P$ transition in HeI (see Fig. 31) is induced by this field and the ratio of the signal from that line (6632 Å) to the emission at the associated allowed $3^1D - 2^1P$ line (6678 Å) is an increasing function of the ion-wave field. Figure 30(d) shows a backscattered signal (upper trace) and forbidden line signal, and time correlation of the latter with the former is observed. Though not shown in this photograph, the second spectroscopic channel may monitor the continuum or allowed line to guarantee that the enhanced emission is indeed due to the forbidden transition.

Shot-to-shot frequency scans of the backscattered radiation have been made in plasmas of He, A, and H_2 and may be seen in Fig. 32. Z_{eff} may be inferred from spectroscopically determined densities to be 1, 2, and 8 for for H_2, He, and A respectively; $\gamma_e = 1$ and $\gamma_i = 3$ from physical arguments; T_e/T_i from computer simulation of our plasma to be $\sim$ 2.5, 3, and 7 for the three gases respectively. Hence, one may assign electron temperatures to the observed red shifts of the scattered light if the shift is due to acoustic waves: T_e = 45, 55, 130 eV for H_2, He, and A respectively.

As diagnostics of the laser-altered plasma were not sufficient to pin down the temperatures in the focus and show agreement with these red shifts in the scattered light, a computer code was developed on the UCLA campus Computing Network's IBM System/360-91 to calculate the time evolution of plasma parameters. Included in the model were: 1) inverse Bremsstrahlung heating of the electrons by the laser; 2) collisional energy transfer between electrons and ions; 3) electron and ion heat conduction; 4) hydrodynamic expansion of the heated plasma into the regions of cold background plasma; 5) ionization and recombination between ion species up to Z = 8 for A; and

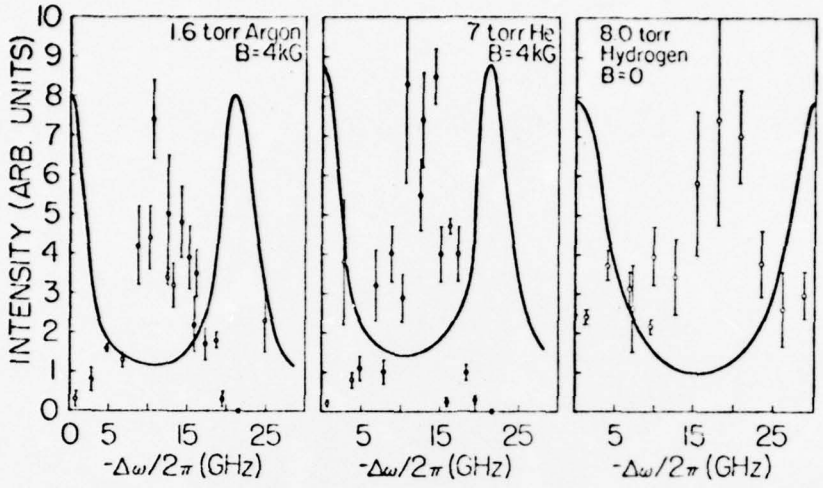

Fig. 32 Intensity of backscattered light vs. redshift. Bars indicate probably error of mean of several shots. Curves are scans of stray light and indicate finesse and free spectral range of interferometer.

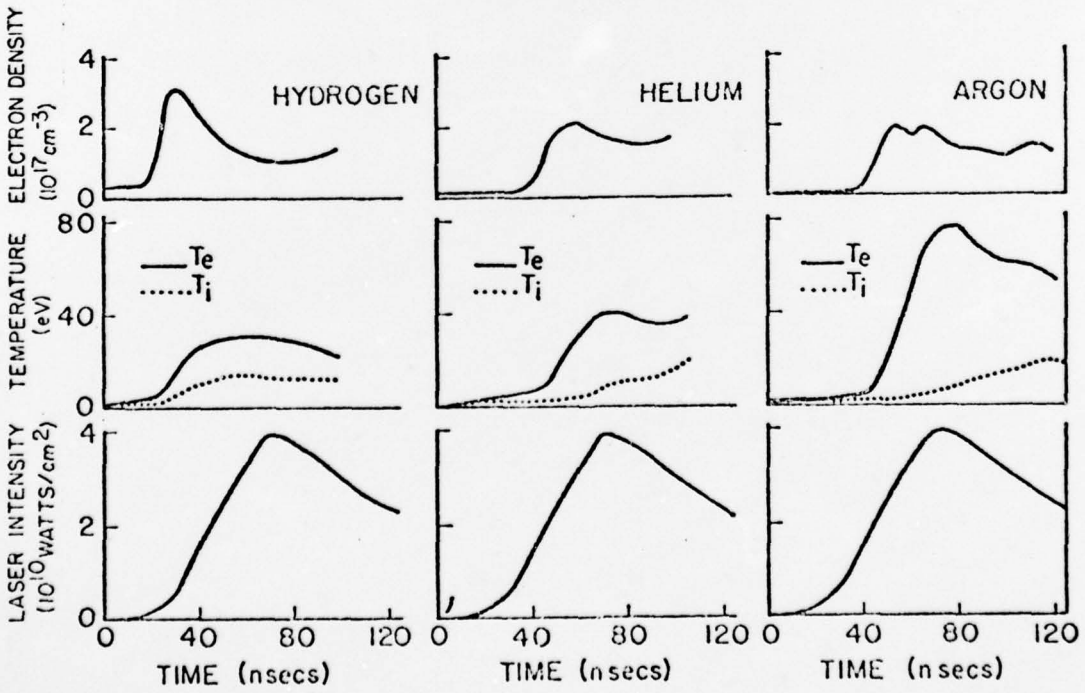

Fig. 33 Temperoal evolution of plasma parameters obtained from computer simulation.

6) modification of collisional transport processes to include contributions from multiple ion species including neutrals. Results of the calculation were found to be in agreement with other codes in the literature when the processes included were the same, though none of those included all processes listed above. The temporal evolution of T_i, T_e, n_e and the laser intensity obtained from the computer simulation is shown in Fig. 33 for each of the three gases. As suspected from experimental observations, the code predicted a short period of modest heating followed by avalanche ionization and stronger heating with peak electron temperature occuring shortly after peak laser intensity at the optimal time for backscattering. As indicated in Fig. 34 the absolute values of the peak electron temperature were lower than those implied by the scattering spectra, though the variation with filling gas is similar.

Finally, we can compare the absolute magnitude of the threshold in the theory. From the intensity of backscattered light (about 50 W), one can infer that the excited ion waves have amplitudes about 9 or 10 e-foldings above the thermal level. The finite-interaction-length theory predicts the laser intensity necessary to achieve a given number of e-foldings. This intensity depends on the ion Landau damping rate and is shown in Fig. 35 as a function of T_e (actually, T_e/T_i), for various densities. Since the density at the focal spot after ionization by the beam is measured to be about 10^{17} cm^{-3}, it is seen that even our peak intensity is below threshold if no electron heating takes place. However, when the electrons are heated to the temperatures measured and calculated, the T_e/T_i ratio increases, and the threshold drops so that backscattering can occur even in the tail of the pulse, as we observe. This threshold intensity is much higher than that for homogeneous plasmas or for inhomogeneous plasmas with long temperature scale lengths (as in our case)

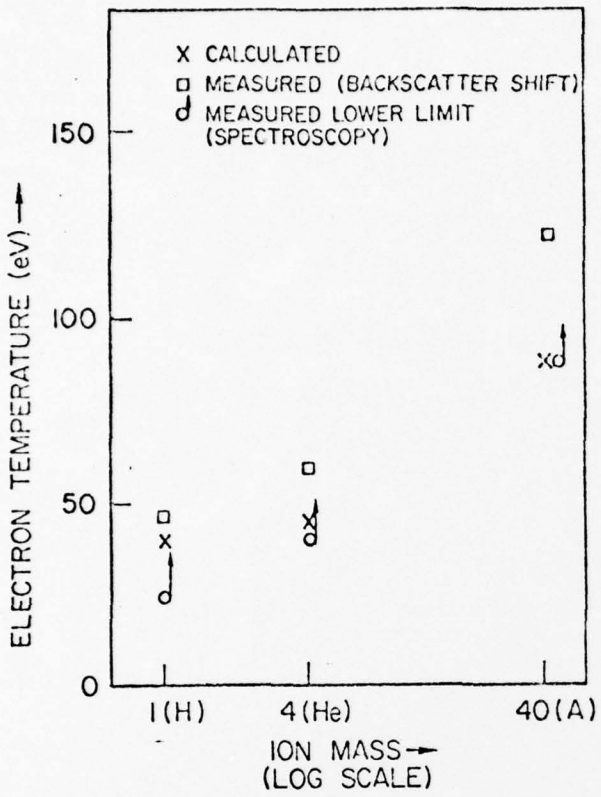

Fig. 34 Electron temperature as a function of ion mass.

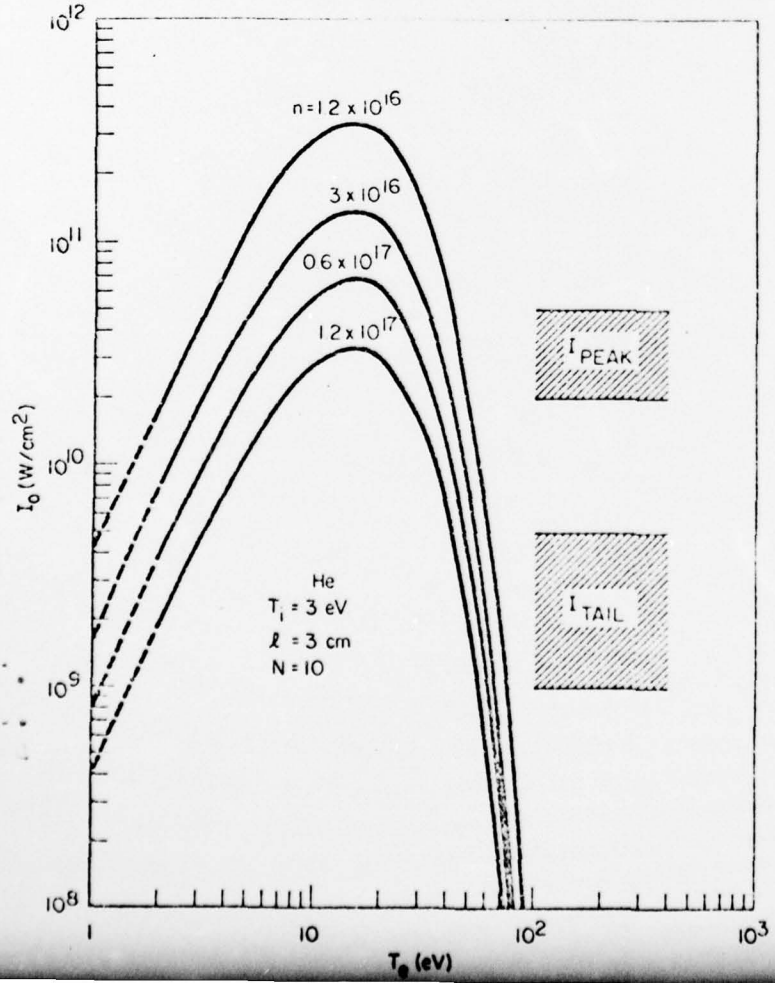

Fig. 35 Theoretical threshold intensity I_o vs. KT_e for various n_e. The ranges of experimental values of I_o in the peak and the tail of the pulse are shown.

and therefore gives credence to the basic correctness of the finite-length corrective threshold. Although SBS has been seen also in other experiments, this is the only one in which the results are consistent with excitation starting from the thermal fluctuation level.

ACKNOWLEDGMENTS

The author wishes to express his appreciation to his coworker S. P. Obenschain for allowing him to present unpublished data from their finite bandwidth experiment. This material is based in part on a dissertation being submitted by S. P. Obenschain to the University of California in partial fulfillment of the requirements for the Ph.D. degree. He also wishes to thank F. F. Chen, M. Herbst and J. Turechek for providing him with the information on their CO_2 laser stimulated Brillouin scattering experiment. The work described in this review was supported in part by the U.S. Air Force Office of Scientific Research, Contract F49620-76-C-0012, the U.S. Energy Research and Development Administration, Contract E(04-3)-34, P.A. 236 and the National Science Foundation, Grant ENG 75-14452.

References

1. K. Nishikawa, J. Phys. Soc. Jap. 24. 916 (1968); 24, 1152 (1968).

2. J. H. Nuckolls, in Laser Interaction and Related Plasma Phenomena Plenum, New York, 1974), Vol. 313.

3. J. J. Thomson, Nuclear Fusion 15. 237 (1975).

4. E. J. Valeo and C. R. Oberman, Phys. Rev. Lett. 30. 1035 (1973).

5. J. J. Thomson and J. I. Karush, Phys. Fluids 17, 1608 (1974).

6. G. E. Vekshtein and G. M. Zablavskii, Sov. Phys. Doklady 12. 34 (1967).

7. G. M. Zablauskii and U. S. Zakharov; Sov. Phys.-Tech. Phys. 12, 7 (1967).

8. S. Tamor, Phys. Fluids 16, 1169 (1973).

9. J. J. Thomson, W. L. Kruer, S. E. Bodner and J. S. DeGroot, Phys. Fluids 17, 849 (1971).

10. G. Laval, R. Pellat and D. Pesme, Phys. Rev. Lett. 36, 192 (1976).

11. C. Yamanaka, T. Yamanaka, T. Sasaki and J. Mizui, Phys. Rev. Lett. 32, 1038 (1974).

12. D. Arnush, K. Nishikawa, B. D. Fried, C. K. Kennel, and A. Y. Wong, Phys. Fluids 16, 2270 (1973).

13. C. W. Murphy, I. Alexeff, S. Aihara, H. Ikegami, Bull. Am. Phys. Soc. 18, 1295 (1973).

14. R. B. Spielman, J. S. DeGroot, and D. A. Rasmussen, J. Appl. Phys. 47 1909 (1976).

15. R. Stenzel and A. Y. Wong, Phys. Rev. Lett. 28, 274 (1972).

16. H. C. Kim, R. L. Stenzel and A. Y. Wong, Phys. Rev. Lett. 33, 886 (1974).

17. J. M. Kindel, K. Lee and E. L. Lindmann, Phys. Rev. Lett. 34, 134 (1975).

18. J. F. Drake, P. K. Kaw, Y. C. Lee, G. Schmidt, C. S. Liu, and M. N. Rosenbluth, Phys. Fluids 17, 778 (1974).

19. M. N. Rosenbluth, Phys. Rev. Lett. 29, 565 (1972); M. N. Rosenbluth and R. Z. Sagdeev, Comments on Plasma Physics and Controlled Fusion 1, 129 (1972); C. S. Liu, M. N. Rosenbluth, and R. B. White, Phys. Rev. Lett. 31, 697 (1973) and Phys. Fluids 17, 1211 (1974); M. N. Rosenbluth, R. B. White, and C. S. Liu, Phys. Rev. Lett. 31, 1190 (1973); D. Pesme, G. Laval, and R. Pellat, Phys. Rev. Lett. 31, 203 (1973); R. W. Harvey and G. Schmidt, Phys. Fluids 18, 1395 (1975).

20. D. W. Forslund, J. M. Kindel, and E. L. Lindman, Phys. Rev. Lett. 30, 739 (1973), Phys. Fluids 18, 1002 (1975) and 18, 1017 (1974); D. F. DuBois D. W. Forslund, and E. A. Williams, Phys. Rev. Lett. 33, 1013 (1974); D. Biskamp and H. Welter, Phys. Rev. Lett. 34, 312 (1975); W. L. Kruer, K. G. Estabrook, and K. H. Sinz, Nucler Fusion 13, 779 (1973).

21. F. F. Chen, Laser Interaction and Related Plasma Phenomena, ed. by H. J. Schwarz and H. Hora (Plenum Press, New York, 1973), 3A, 291.

Unclassified

SECURITY CLASSIFICATION OF THIS PAGE (When Data Entered)

(19) REPORT DOCUMENTATION PAGE	READ INSTRUCTIONS BEFORE COMPLETING FORM
1. REPORT NUMBER (18) AFOSR - TR-77-0157 ✓	2. GOVT ACCESSION NO.
3. RECIPIENT'S CATALOG NUMBER (9)	
4. TITLE (and Subtitle) (6) EXPERIMENTAL SIMULATION OF PARAMETRIC INSTABILITIES IN LASER-PLASMA INTERACTIONS	5. TYPE OF REPORT & PERIOD COVERED Scientific-Interim rept.
	6. PERFORMING ORG. REPORT NUMBER
7. AUTHOR(s) (10) N. C. Luhmann, Jr.	8. CONTRACT OR GRANT NUMBER(s) (15) F49620-76-C-0012 new ✓ NSF-Eng-75-14452
9. PERFORMING ORGANIZATION NAME AND ADDRESS University of California Electrical Sciences and Engineering Department ✓ Los Angeles, California 90024	10. PROGRAM ELEMENT, PROJECT, TASK AREA & WORK UNIT NUMBERS (16) 9751-03 (17) 61102F (12) 43 p.
11. CONTROLLING OFFICE NAME AND ADDRESS (11) Air Force Office of Scientific Research/NP Bolling AFB, DC 20332	12. REPORT DATE Nov[illegible]76
	13. NUMBER OF PAGES 41
14. MONITORING AGENCY NAME & ADDRESS (if different from Controlling Office)	15. SECURITY CLASS. (of this report) UNCL/UNCL
	15a. DECLASSIFICATION/DOWNGRADING SCHEDULE

16. DISTRIBUTION STATEMENT (of this Report)

Approved for Public Release; Distribution Unlimited

17. DISTRIBUTION STATEMENT (of the abstract entered in Block 20, if different from Report)

18. SUPPLEMENTARY NOTES

TECH, OTHER

19. KEY WORDS (Continue on reverse side if necessary and identify by block number)

20. ABSTRACT (Continue on reverse side if necessary and identify by block number)

There is currently a great interest in the mechanisms by which intense electromagnetic radiation interacts with plasmas. A major impetus for this interest has been the laser-pellet fusion program. The process whereby the incident electromagnetic wave gives up energy to the plasma can be much more complex than simple binary collisional damping by electronion collisions.

DD FORM 1 JAN 73 1473 EDITION OF 1 NOV 65 IS OBSOLETE 409 432 Unclassified

SECURITY CLASSIFICATION OF THIS PAGE (When Data Entered)